

ARTICLE OPEN



Transparent flexible thin-film p - n junction thermoelectric module

Xizu Wang¹✉, Ady Suwardi¹, Siew Lay Lim¹, Fengxia Wei¹ and Jianwei Xu^{1,2}✉

Transparent and flexible thermoelectrics has been highly sought after for future wearable devices. However, the main stumbling block to prevent its widespread adoption is the lack of p -type transparent thermoelectrics and the stringent criteria of electrical and thermal properties matching appropriately between p -legs and n -legs. This work demonstrates the fabrication of p -type PEDOT:PSS films whose optical properties, electrical conductivity, thermal conductivity, and Seebeck coefficient were engineered to perfectly match the n -type indium tin oxide (ITO) counterparts. The dense p -type PEDOT:PSS and n -type ITO thin films show a thermoelectric figure of merit of $zT = 0.30$ and 0.29 at 450 K, and a thermal conductivity of 0.22 and 0.32 $\text{W m}^{-1} \text{K}^{-1}$, respectively. A flexible thermoelectric generator (TEG) module with a high transmittance of $>81\%$ in the visible wavelength range of 400 – 800 nm is fabricated using 10 pairs of p -type PEDOT:PSS and n -type ITO thin film legs. An ultra-high power density of 22.2 W m^{-2} at a temperature gradient of 80 K was observed, which is the highest power density reported for organic/hybrid-based flexible TEGs so far. Our transparent flexible thin-film p - n junction thermoelectric module with exceptionally high power generation may take a tremendous step forward towards multi-functional wearable devices.

npj Flexible Electronics (2020)4:19; <https://doi.org/10.1038/s41528-020-00082-9>

INTRODUCTION

As the size of our modern consumer electronics gets smaller, the waste heat generated from the energy conversion processes inevitably grows larger. The ubiquity of these so-called low-grade waste heat (<200 °C) presents multifold challenges in thermal management and energy efficiency. Thermoelectric materials, which convert heat to electricity and vice versa, have the potential to be a one-stop solution for both cooling and waste heat harvesting. In order to integrate thermoelectrics into existing devices, flexibility and sometimes transparency are of paramount importance due to the fact these two features are necessary for a plethora of small-sized consumer electronics, internet-of-things, and wearable devices. As a matter of fact, most of the state-of-the-art thermoelectrics belongs to inorganic chalcogenides, half-heuslers, or silicides, which are opaque due to their small band-gaps^{1–6}. A few emerging wide band-gap thermoelectrics, such as AZO (Al:ZnO), ITO (In:SnO₂), CuAlO₂, and CuI thin films have been reported to possess high transparency but often suffer from low performances^{7–11}.

In recent years, tremendous progresses have been achieved in discovering and enhancing the performance of flexible thermoelectrics which were either made of all-organic, hybrid organic–inorganic, or inorganic compounds integrated on flexible substrates^{12–21}. Most of the reports on flexible thermoelectrics involves either poly(3,4-ethylenedioxythiophene):poly(styrene-sulfonate) (PEDOT:PSS), polyaniline (PANI), or polypyrrole (PPY)-based polymers with various doping or chemical modifications^{22–27}. In terms of flexible thermoelectric generator (TEG) devices, high power density of more than 10 $\mu\text{W cm}^{-2}$ have been consistently reported in the past few years, most of which involves inorganics, such as Te-nanorods, single-walled carbon nanotube (SWCNT), TiS₂, or Cu₂Se as the pairing legs^{28–34}.

Nonetheless, further combining flexibility with transparency has proven to be an arduous task, as evident from the lack of reports

on transparent flexible thermoelectrics, especially p -type¹¹. A big obstacle in engineering multi-functional thermoelectrics lies in the fact that thermoelectric modules are composed of coupled p -type and n -type legs electrically connected in series, and thermally in parallel. In other words, the device performances are always limited by the leg with low performance. Therefore, designing transparent flexible thermoelectrics necessitates the confluence of optical, mechanical, and thermoelectric performance matching for both p -type and n -type legs³⁵.

In this work, we report a TEG module that is both transparent and flexible while at the same time retaining good thermoelectric performances in both p -type and n -type legs. The p -type leg made up of PEDOT:PSS thin film was post-treated by trifluoromethanesulfonic acid (CF₃SO₃H, TFMS) to achieve high electrical conductivity and Seebeck coefficient¹³. Correspondingly, the amorphous ITO thin film, which was optimized by controlling the deposition oxygen and hydrogen partial pressures, was adopted as the n -type pairing leg. The optimized electrical conductivity of PEDOT:PSS and ITO reached 2980 and 3094 S cm^{-1} , with corresponding Seebeck coefficients of 21.9 and 20.3 $\mu\text{V K}^{-1}$ and thermal conductivity of 0.22 and 0.32 $\text{W m}^{-1} \text{K}^{-1}$, respectively. The well-matched electronic and thermal properties indicate that PEDOT:PSS and ITO are suitable to be used as a p - n junction pair in transparent flexible TEGs. The TEG module comprises a periodic array of structures of transparent p -type and n -type thermoelectric thin films fabricated on various transparent substrates, such as glass, polyethylene terephthalate (PET), and polycarbonate (PC). The TEG module in this work represents the primary report on multiple legs, fully transparent flexible p - n junction thermoelectric device. In addition, the junctions between the p -type and n -type legs are overlapped on top of each other which precludes the need for external connecting electrodes. This is contrary to traditional thermoelectric devices which typically use metal electrodes, such as silver

¹Institute of Materials Research and Engineering (IMRE), Agency for Science, Technology and Research (A*STAR), #08-03, Fusionopolis Way, Innovis, Singapore 138634, Singapore.

²Department of Chemistry, National University of Singapore, 3 Science Drive 3, Singapore 117543, Singapore. ✉email: wangxz@imre.a-star.edu.sg; jw-xu@imre.a-star.edu.sg

to connect the *p*-type and *n*-type legs. Consequently, the configuration in this work minimizes the energy losses via the contact resistance brought about by the external electrodes, as evident by the high power density of 2.22 mW cm^{-2} , which is amongst the highest reported so far²¹.

RESULTS

Sample preparation and physical properties

PEDOT:PSS is chosen as the *p*-type leg in this work due to its robust thermoelectric performance. The thermoelectric performance of the PEDOT:PSS thin film, with doping or post-treatment has been demonstrated to be comparable to traditional inorganic *p*-type thermoelectric materials^{13,23,35–46}. In our TEG module, we leveraged upon the PEDOT:PSS from our earlier work which used TFMS–MeOH post-treatment to enhance its chemical and thermal stability¹³. The electrical conductivity and Seebeck coefficient of the PEDOT:PSS thin film with TFMS–MeOH post-treatment reaches 2980 S cm^{-1} and $21.9 \mu\text{V K}^{-1}$, respectively. On the other hand, indium tin oxide (ITO) was used as the *n*-type counterpart in our device. It is a commonly used materials for a wide range of applications ranging from solar cells to optoelectronics. In addition, it has high transparency in the visible light region because of its wide band gap. Furthermore, owing to its highly degenerate *n*-type nature, it has very high electrical conductivity, making it a good potential material for transparent thermoelectrics^{47,48}. Nevertheless, the main hindrance to its widespread adoption in flexible devices lies in the fact that good quality ITO thin films require high processing temperature exceeding 200°C , which makes it difficult to integrate into flexible substrates such as PET. In addition, its Seebeck coefficient is far from optimized because of its tendency to possess excessive electrons. Therefore, adoption of ITO for flexible applications may rely on counter-doping to maximize the thermoelectric properties and process it at near-room temperature.

In order to control and optimize the carrier concentration of ITO, process parameters such as the hydrogen partial pressure need to be delicately controlled. It has been reported that the magnitude of the hydrogen partial pressure during film deposition can strongly influence the number of oxygen vacancies formed, and hence the carrier concentration, mobility, and electrical conductivity in ITO^{27,28}. Therefore, tuning the sputtering process parameters enables us to study the electronic transport mechanisms in ITO.

In this work, the ITO thin films were deposited in various atmospheres ranging from pure argon (Ar) to a mixture of hydrogen and argon (H1, H2), oxygen and argon (O1, O2, O3), as shown in Table 1. The elemental chemical states and bonding of the ITO thin films were investigated using X-ray photoelectron spectroscopy (XPS), as shown in Fig. S1. The binding energies of the In $3d_{5/2}$ and In $3d_{3/2}$ peaks are ~ 444.5 and 452 eV , respectively. The In $3d_{5/2}$ peaks can be assigned to the In³⁺ species in crystalline In₂O₃. The absence of peaks or shoulders at 443.6 eV indicates the absence of the elemental indium phase in all the

films. The binding energies of the In $3d$ and Sn $3d$ peaks are similar for all the ITO thin films, which suggests that the formation of interstitial metallic atoms does not occur as a result of the different deposition conditions. The cut-off energies for all the ITO thin films are close to that of the commercial ITO, indicating similar work functions. Hence, the introduction of hydrogen in the gas mixture during the sputtering process seems to only affect the oxygen deficiency in ITO films, which affects its stoichiometry.

To elucidate the effect of different sputtering gas mixtures on the ITO film morphologies, atomic force microscopy (AFM) was used to image the commercial ITO and the ITO thin films, as shown in Fig. S2. Comparatively, the ITO films show a smaller grain size as evident from smaller value of root-mean-square surface roughness (R_q) than the polycrystalline commercial ITO. The roughness values (R_q) for the commercial ITO, H2, H1, Ar, O1, O2, O3 are 3.8, 0.6, 1.6, 0.9, 0.5, 0.7, 0.5 nm, respectively. Thus, the introduction of various mixture of gases during the sputtering process results in smooth film morphologies, which may be attributed to a lower degree of crystallinity in the sputtered films compared to the commercial ITO, as evident from the broader X-ray diffraction (XRD) spectra peaks of sputtered films as compared with the commercial ITO shown in Fig. 1a. This low-crystallinity nature is expected because of the low substrate temperature during sputtering (60°C) and the absence of lattice matching on amorphous glass substrates.

For the ITO (oxygen–argon) samples, a higher intensity peak is observed at $2\theta = 24^\circ$ as compared to $2\theta = 31^\circ$. On the other hand, for the ITO (hydrogen–argon) samples, the peak with highest intensities occurs at $2\theta = 31^\circ$. The relatively sharper peak from ITO (hydrogen–argon) compared with ITO (oxygen–argon) samples reveals better crystalline quality of the samples grown under hydrogen/argon atmosphere. From Fig. 1c, it appears that the presence of argon or hydrogen in the process gas mixture enhances the formation of the (222) plane, which is related to the 2D metal–oxide network structure. This 2D network structural change in the crystallinity of ITO is expected to affect the overall electrical properties of the films, as shown in Fig. 2. In contrast, the ITO with oxygen–argon gas mixture shows the enhanced formation of the (211) plane (Fig. 1b) associated with the 1D metal–oxide structure of ITO crystal, which may increase the interface/dislocation scattering in the ITO film. Furthermore, based on XRD spectra in Fig. 1a, the distinct peaks at 2θ of 24° and 31° in commercial ITO correspond to the lattice *d*-spacing of 2.9683 \AA [(222)] and 4.1225 \AA [(211)], respectively. For the sputtered films, the shifts in these two peaks indicate that the *d*-spacings for the (222) and (211) planes of the thin film have decreased to 2.7851 and 3.8212 \AA , respectively, as illustrated in Fig. 1b, c.

Electronic and thermoelectric properties

The room temperature electrical conductivity, carrier concentration and mobility of ITO films deposited with pure argon (Ar), hydrogen–argon (H1, H2), and oxygen–argon (O1, O2, O3) gas mixtures as a function of the reactive gas partial pressure are shown in Fig. 2. In Fig. 2a, the use of hydrogen–argon mixtures slightly increased the electrical conductivity of ITO films compared with the film grown in pure argon. On the contrary, the introduction of oxygen–argon mixtures significantly reduced electrical conductivity by more than two orders of magnitude. This can be ascribed to the reduction of oxygen vacancies in the sputtered films, which results in a lower carrier concentration, as shown in Fig. 2b⁴⁹. In addition, the carrier mobility of the ITO films is lowered with the addition of mixing gases, especially oxygen, which shows dramatic reduction with increasing oxygen partial pressure. Owing to the influence of mixing gas type as well as its partial pressure on both the carrier concentration and carrier mobility, the electrical conductivity can be sensitively tuned by carefully controlling the gas mixtures during deposition.

Table 1. The sputtering condition of all ITO and their thickness.

ITO films	Gas ratio	Pressure (Pa) & temperature ($^\circ\text{C}$)	Thickness (nm)
ITO–H1	Ar:Ar + H ₂ ^a = 14:2	0.4–0.5; 50	130
ITO–H2	Ar:Ar + H ₂ ^a = 14:1	0.4–0.5; 50	130
ITO–Ar	Ar = 14	0.3–0.4; 50	126
ITO–O1	Ar:O ₂ = 14:0.05	0.3–0.4; 50	90
ITO–O2	Ar:O ₂ = 14:0.1	0.3–0.4; 50	80
ITO–O3	Ar:O ₂ = 14:0.2	0.3–0.4; 50	70

^aAr:H₂ is 95:5.

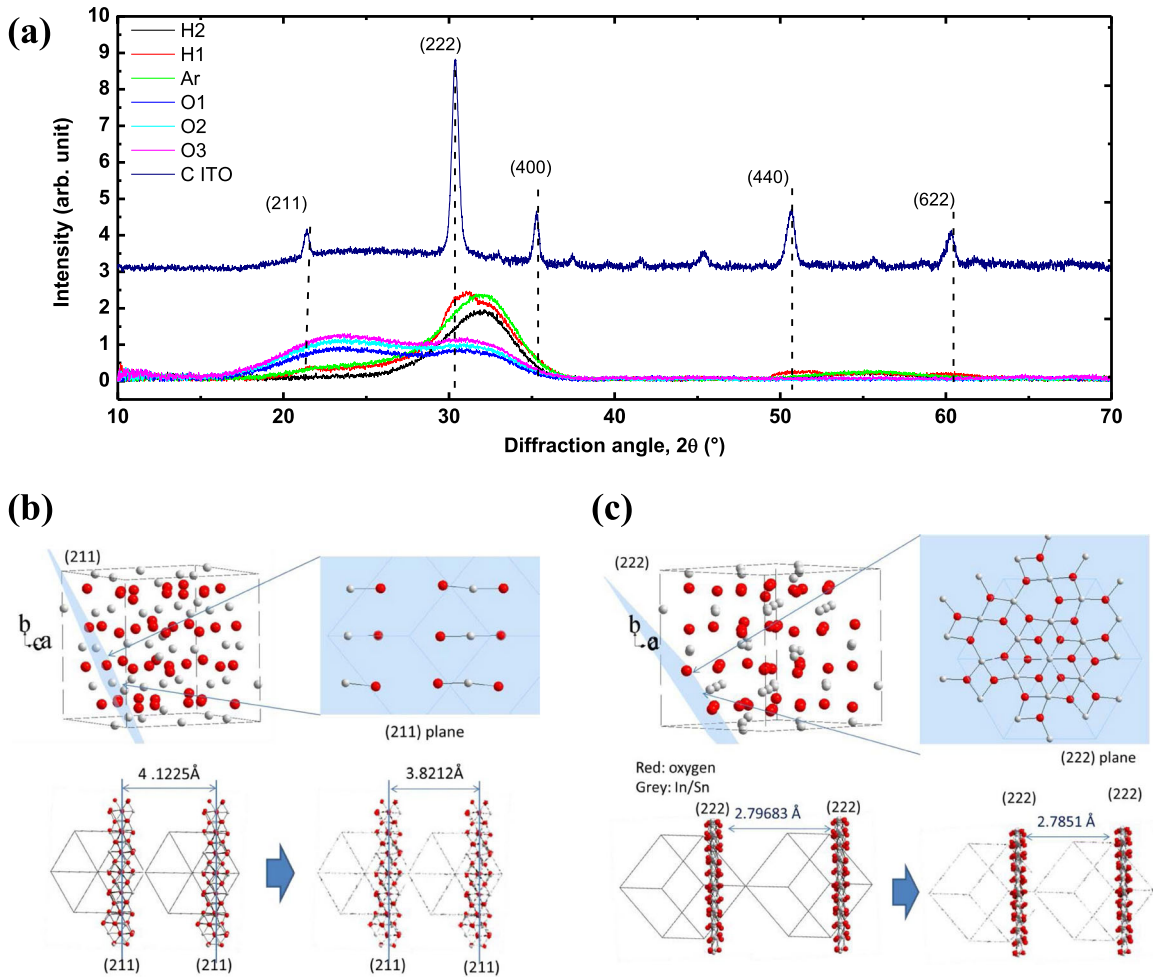


Fig. 1 Phase and structural characterization of the ITO thin films. **a** X-ray diffraction (XRD) spectra of ITO films grown on glass substrates under a pure argon environment, or at different hydrogen or oxygen partial pressures, compared with the commercial ITO. Diagrams illustrating the changes in the nano-structural arrangement in **b** the 1D structure of the (211) plane and **c** the 2D structure of the (222) plane.

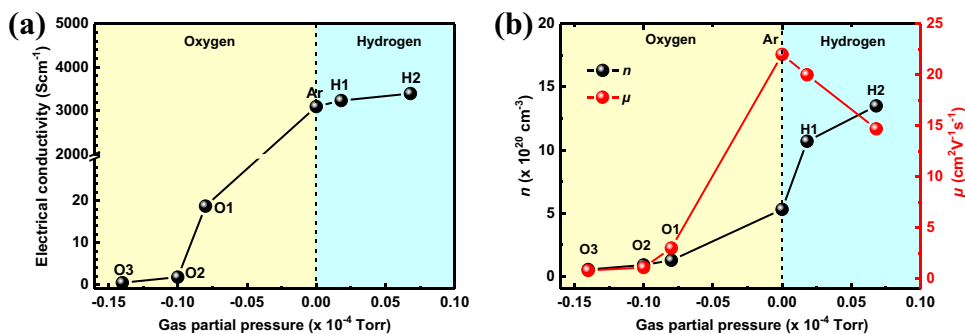


Fig. 2 Electrical properties of thin films grown under different conditions. **a** Room temperature electrical conductivity. **b** Carrier concentration (n) and mobility (μ) of ITO films deposited under a pure argon environment, or at different hydrogen or oxygen partial pressures.

Figure 3 shows the temperature dependence electrical conductivity, Seebeck, power factor, and thermal conductivity of ITO films deposited under different gas mixtures. In Fig. 3a, similar to the commercial ITO, the ITO thin films deposited using Ar, H1, and H2 show decreasing electrical conductivity with increasing temperature, which is the signature of metallic/nondegenerate

semiconductor behavior. In contrast, the electrical conductivity of the thin films deposited with O1, O2, and O3 shows an increasing trend at temperature beyond 350 K, which can be attributed to thermal-activated oxygen vacancies. Accordingly, the Seebeck coefficients (Fig. 3c) for O1, O2, and O3 are comparatively much higher than the Ar, H1, and H2 films due to the low carrier

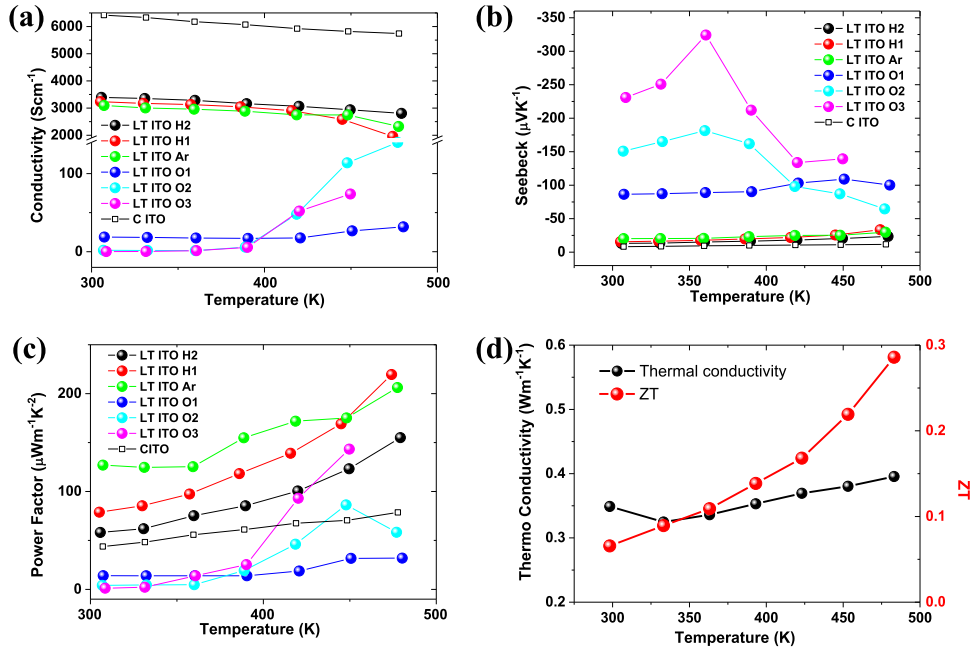


Fig. 3 Thermoelectric properties of ITO films deposited under a pure argon environment, or at different hydrogen or oxygen partial pressures. a Electrical conductivity, **b** Seebeck coefficient, and **c** power factor (PF), as a function of temperature. **d** The thermal conductivity (TC) and figure-of-merit zT of the ITO thin film sample Ar, as a function of temperature.

concentration, which is consistent with the following Mott's relation:

$$S = \frac{8\pi^2 k_B^2 T}{3eh^2} m^* \left(\frac{\pi}{3n}\right)^{2/3} \quad (1)$$

Figure 3c shows the temperature dependence power factor which shows highest values for Ar-deposited ITO thin films for almost the entire temperature range, which can be credited to the high carrier mobility for thin film grown under the inert argon atmosphere as opposed to those grown under gas mixtures. Furthermore, the thermal conductivity (k) of the ITO thin film deposited under Ar atmosphere remains low at $0.32\text{--}0.40\text{ W m}^{-1}\text{ K}^{-1}$ from 300 to 480 K, respectively. This is much lower than the reported k of $4\text{ W m}^{-1}\text{ K}^{-1}$ for the commercial ITO and among the lowest reported for oxides⁵⁰. The low thermal conductivity can be ascribed to a lower degree of crystallinity since the thin film was sputtered at room temperature. Consequently, the figure-of-merit zT increases from 0.07 to 0.29 over the same temperature range as shown in Fig. 3d.

Transport mechanism modeling

Figure 4 shows the electronic properties of the ITO thin films as a function of carrier concentration n at room temperature. The carrier mobility vs. concentration profile shown in Fig. 4a represents the signature of dislocation scattering-limited transport, similar to the one observed in GaN thin films⁵¹. The black, red, and purple dotted lines represent increasing dislocation density, which results in more carrier scattering, and thus lowers mobility. Within each dotted line, increasing the carrier concentration results in increased mobility, which can be associated to lower thermal activation energy for carrier mobility than carrier concentration⁵¹. Pisarenko plot based on Boltzmann transport equations (Eqs. (2) and (3)) shows ionized-impurities scattering transport ($r = 1.5$) for the three samples with lowest carrier concentration (O1, O2, and O3), as shown in Fig. 4b. On the contrary, the H1, H2, and Ar samples can be fitted to acoustic phonon scattering transport ($r = -0.5$) with an effective mass of $0.35m_0$, which was confirmed by transport coefficients plot based on Snyder–Kang model, as shown in Fig. 4c⁵². It is worth mentioning that the relatively low effective

mass in these samples contributes to higher mobility, and hence higher power factor and zT ⁵³.

$$S = \pm \frac{k_B}{e} \left[\eta - \frac{(r + 2.5)F_{r+1.5}(\eta)}{(r + 1.5)F_{r+0.5}(\eta)} \right] \quad (2)$$

$$n = \frac{N_v}{2\pi^2} \left(\frac{2k_B T m^*}{\hbar^2} \right)^{3/2} F_{0.5}(\eta) \quad (3)$$

The difference in scattering mechanisms between samples with low carrier concentrations (O1–O3) and the ones with high carrier concentration (H1, H2, Ar) qualitatively explains the occurrence of mobility plateau for carrier concentration of around 10^{20} cm^{-3} (the sample deposited in Ar atmosphere). Consequently, the same sample also has the higher zT as compared to films deposited using other gas mixture ratios, as shown in Fig. 4d, with maximum zT of 0.29, which is comparable to the p -type PEDOT:PSS film ($zT = 0.30$).

The room temperature zT versus optical band-gap (E_g) of ITO and PEDOT:PSS thin films was compared with those of typical thermoelectric materials in Fig. 5⁷. At 480 K, we observed that the zT of ITO in this work was the highest amongst all the n -type materials in the transparent range ($E_g > 3\text{ eV}$), and was similar to the best reported zT for transparent thermoelectric material (p -type $\gamma\text{-CuI}$)¹¹. In terms of performance, there is plenty of scope for further work to obtain ITO with better thermoelectric properties, such as optimizing the carrier concentration in the range of $1\text{--}5 \times 10^{20}\text{ cm}^{-3}$ through careful control of the film deposition process.

Transparent p - n junction TEG module

In order to optimize the output power of a TEG module, ensuring a suitable pairing of the p -type and n -type legs is very important. The optimal device geometry can be defined as

$$\frac{L_n A_p}{L_p A_n} = \left(\frac{\rho_p \kappa_n}{\rho_n \kappa_p} \right)^{1/2} \quad (4)$$

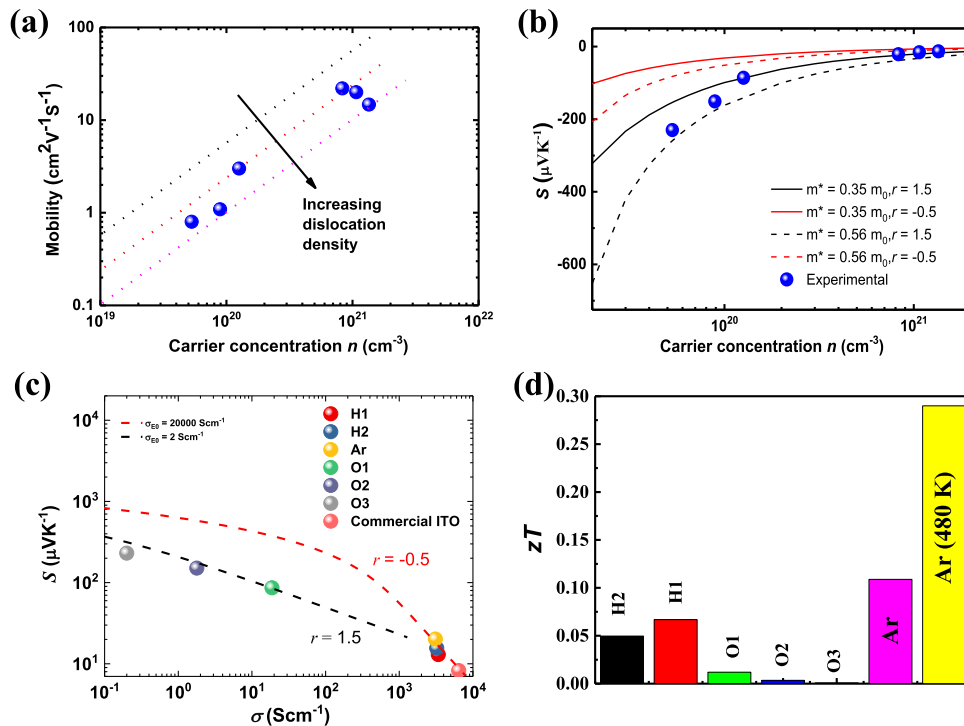


Fig. 4 Thermal and electrical properties of the ITO thin film (130 nm) sputtered on polished glass. **a** Electron mobility vs. carrier concentration (n), **b** Seebeck coefficient (S) vs. carrier concentration (n), **c** Seebeck vs. electrical conductivity and **d** figure-of-merit (zT) for samples sputtered in different atmospheres.

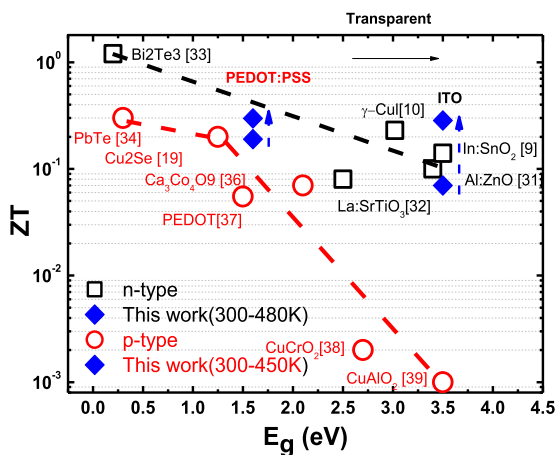


Fig. 5 Figure-of-merit zT of reported n - and p -type thermoelectric materials at room temperature versus energy bandgap, compared with this work. Notably, the zT values of n -type ITO and p -type PEDOT:PSS thin film in this work are adjusted to a similar level to achieve a high-performance flexible TE module with high transparency.

where L , A , ρ , and κ represent the length, area, electrical resistivity, and thermal conductivity of the respective legs. It is evident from Eq. (4) that in order to have a TEG module with a balanced size (i.e. similar geometry between p -type and n -type legs), it is important to choose materials with similar magnitudes of both electrical and thermal conductivity. Figure 6a shows the electrical conductivity and Seebeck coefficient versus temperature from 300 to 450 K. Evidently, both the magnitudes of electrical conductivity and Seebeck coefficient of PEDOT:PSS match those of ITO thin films,

respectively, and both of PEDOT:PSS and ITO exhibit similar trends to the temperature, ensuring to give optimal performance of TEG module throughout the entire temperature range. The comparison of thermoelectric properties of treated PEDOT:PSS and ITO (Ar) to flexible TEG modules from the literatures are listed in Table 2. Remarkably, the TEG module in this work shows the highest output power density amongst organic/hybrid-based flexible TEG. In addition, the output power density is of the same magnitude as fully inorganic-based flexible TEG modules.

The structure of the TEG module in this work is illustrated in Fig. 6b. The ITO (H1) thin film is able to function as both the n -type thermoelectric leg and the overlay contact bridge in a transparent, in-plane TEG that utilizes the treated PEDOT:PSS thin film as the p -type thermoelectric leg, without the need for additional electrodes. The thermoelectric modules fabricated with ITO (Ar) thin film and treated PEDOT:PSS thin film as the n -type and p -type thermoelectric legs, respectively, on both glass and PET substrates were highly transparent, with a similar optical transmittance of 84% over the visible and near infrared regions (350–1100 nm, as shown in Fig. 6c, d). The TEG module fabricated on PET also possesses good flexibility and mechanical stability. The internal resistance of the module was reduced by about 3% after 10,000 tensile bending cycles (the bending angle up to 130°), as shown in Fig. S3b, indicating that the module was suitable for use in wearable and other applications where repeated bending was required. The electrical output of the TEG module on glass, formed by connecting 10 pairs of p -type and n -type thermoelectric legs in series, were studied at temperature differences (ΔT) ranging from 5 to 80 K, as shown in Fig. 6e, f. The TEG module generated the maximum power output of 14.3 nW at $\Delta T = 80$ K, with a corresponding power density of 22.2 W m^{-2} . To our knowledge, this is amongst the highest power density from the previously reported transparent thin film TEG module, as illustrated in Fig. 7.

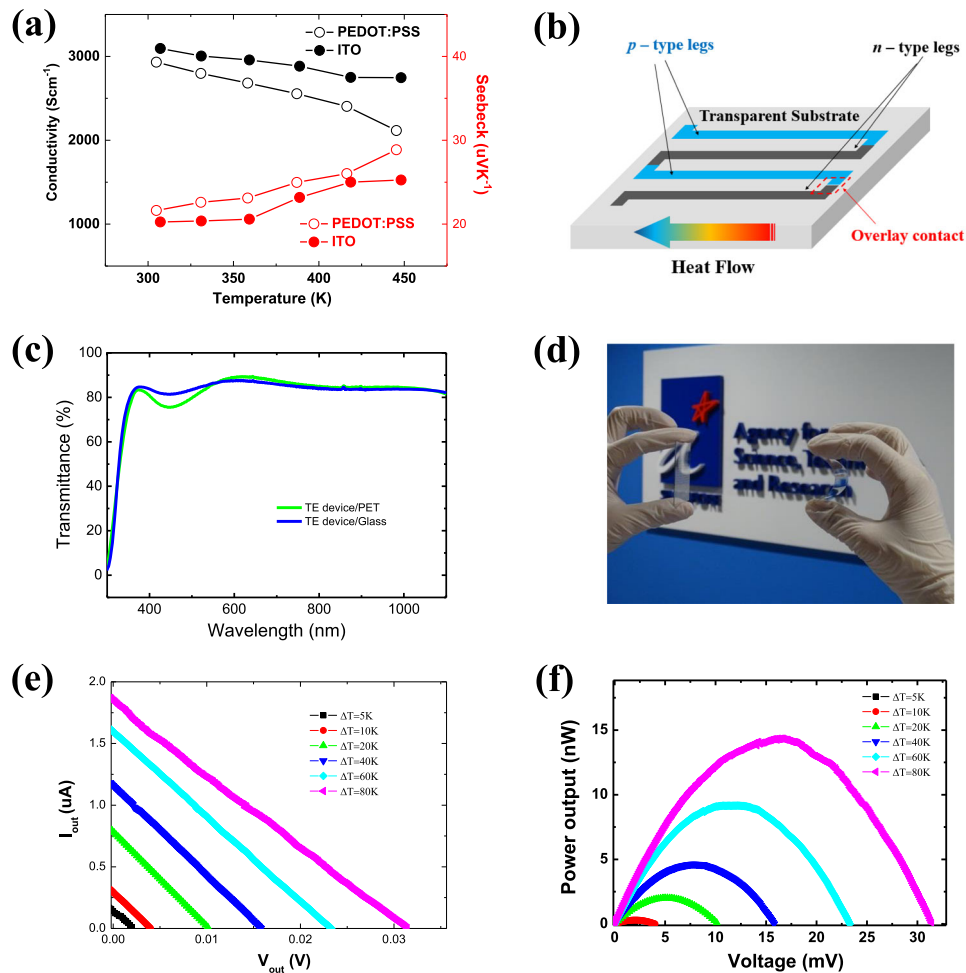


Fig. 6 Device properties of both *p*-type and *n*-type thermoelectrics. **a** Electrical conductivity and Seebeck coefficient of *p*-type PEDOT:PSS thin film, with post-treatment, as a function of temperature. **b** A diagram of an in-plane transparent thermoelectric generator illustrating the basic configuration of *p*-type and *n*-type thermoelectric legs deposited onto a substrate without any electrodes. **c** Transmittance spectra and **d** photo of the thermoelectric module on polyethylene terephthalate (PET) sheets and glass. **e** Output current (I_{out}) and **f** output power (P_{out}) of the thermoelectric module on glass, as a function of output voltage (V_{out}) for different temperature differences.

Table 2. Literature comparison of TEG module performances.

Primary material	Additive/dopant	Remarks	ΔT (K)	Open circuit voltage (mV)	P_{max} ($\mu W cm^{-2}$)	Ref.
PEDOT:PSS + ITO	–	Fully transparent flexible <i>p</i> – <i>n</i> TEG module	80	31	2220	This work
CuI	–	Single leg <i>p</i> -type TEG	10.8	2.5	100	11
PEDOT:PSS	–	Cast solution on polyimide substrate with Ag electrodes	100	7.07	56.8	28
PEDOT:PSS	TiS ₂	PEDOT:PSS–TiS ₂ organic hybrid superlattice films	70	33	250	29
PEDOT:PSS	Te, Cu ₇ Te ₄	8 single legs flexible thermoelectric devices	39	32	39.5	31
PEDOT:PSS	Te nanorods	PEDOT:PSS coated Te nanorods prepared by drop-casting followed by H ₂ SO ₄ treatment	40	13.4	57.2	30
PEDOT:PSS	SWCNT; Te nanorods	H ₂ SO ₄ treatment	44	5.6	21.4	32
PEDOT:PSS	Pristine	Free standing	29	2.0	99	33
PEDOT:PSS	Cu ₂ Se	Nanowire composite thin films	30	15	91	34
Bi _{0.5} Sb _{1.5} Te ₃ /Bi ₂ Te _{2.7} Se _{0.3}	–	Fully inorganic flexible TEG device via screen printing	25.6	700	6320	54
Bi ₂ Te ₃ /Sb ₂ Te ₃	–	Fully inorganic TEG screen printed onto glass fabric	50	90	3800	55

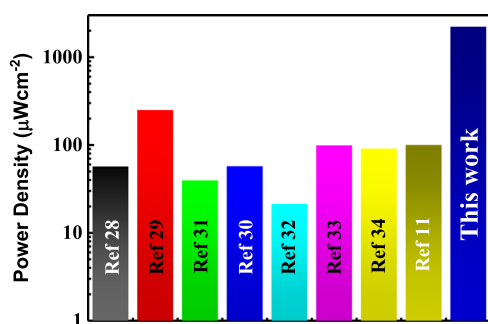


Fig. 7 Power density comparison across literatures for thin-film organic and organic-inorganic hybrid based TEG modules. The power density of the transparent flexible thin-film p - n junction TE module in this work shows almost an order of magnitude higher than those of other organic-based and hybrid-based thermoelectric generator (TEG) modules.

DISCUSSION

As aforementioned, in order to maximize the output power density, the p -type thermoelectric materials should have the comparable electrical and thermal characteristic such as analogous conductivity, Seebeck coefficient and thermal conductivity. In addition to the thermoelectric parameters, the thickness of PEDOT:PSS has to be also properly tuned to be 50 nm to ensure that the film has high transparency in its visible absorption region. On the other hand, the n -type counterpart ITO was purposely fabricated by judiciously controlling its preparation process, such as the temperature, pressure, gas environment with a combination of hydrogen and oxygen ratios in order precisely to match its electrical and thermal parameters as much as possible with its p -type materials. Likewise, its thickness was also controlled to be around 130 nm to make sure that it is transparent with the equivalent transmittance to the PEDOT:PSS film in the visible absorption range. A prototype of transparent flexible p - n junction TEG module was fabricated and the highest thermoelectric power density of 22.2 W m^{-2} at $\Delta T = 80 \text{ K}$ was achieved. This p - n junction TEG module was fabricated by overlaying the treated PEDOT films as the p -type legs and ITO thin films as the n -type counterparts, without the presence of additional connecting electrodes. Both the p -type and n -type legs have comparable electrical conductivity and Seebeck coefficient and thermal conductivity. This type of transparent flexible p - n junction TEG module exhibited good mechanical robustness as evidenced by the <3% reduction in the internal resistance of the module 10,000 tensile bending cycles, offering ITO as an excellent candidate for future applications in thermoelectric power generation, transparent electronics, as well as wearable electronics.

METHODS

Sample fabrication

A 65 nm-thick PEDOT:PSS film used for the p -type thermoelectric leg was prepared using the spin-coating method. A mixture of TFMS and methanol (MeOH) (TFMS–MeOH (V:V = 1:10)), followed by pure methanol was used to treat PEDOT:PSS films. In detail, 200 μL of liquid (TFMS–MeOH) was dropped onto a PEDOT:PSS thin film heated at 130 $^{\circ}\text{C}$. The film was dried for about 30 min, and then the dried film was washed by dipping in methanol for three times. Finally, the 50 nm PEDOT:PSS thin film was obtained and used directly for next-step use. A set of ITO films with different electrical and thermal properties was fabricated by radio frequency magnetron sputtering using a hydrogen–argon or oxygen–argon gas mixture at a process temperature of about 60 $^{\circ}\text{C}$, as shown in Table 1. The most suitable amorphous ITO film was chosen as the n -type thermoelectric leg in the flexible TEG module.

Property characterization

The thicknesses of the PEDOT:PSS and ITO thin films were measured by the KLA Tencor P-16+ Surface Profiler. The carrier concentration and mobility of the thin films were determined using a Hall effect measurement system in Van-der-Pauw geometry with a magnetic field of 0.4 T at room temperature. The electrical conductivity (δ) and Seebeck coefficient (S) were measured simultaneously under helium backfilled vacuum condition with a ZEM3-HR (from ULVAC RIKO) system with Ni contacts and thermocouples and electrodes in a reversed vertical arrangement. The thermal conductivities of the thin films were measured using the pulsed laser heating thermoreflectance method with a rear heating and front detection (RF) configuration (NanoTR system from NETZSCH)²⁶. The specific heat capacity was measured by differential scanning calorimeter (Mettler Toledo).

The transmittance spectra were obtained on an UV–Vis–NIR spectrophotometer (Shimadzu UV–Vis spectrophotometer UV-3600). The TEG module was fabricated using spin coating and sputtering methods on glass and PET substrates. XPS measurement was performed on a theta probe angle-resolved X-ray photoelectron spectrometer (ARXPS) System (Thermo Scientific) at a base pressure of 1×10^{-9} Torr and a step size of 0.1 eV using monochromated, micro-focused Al K-Alpha X-ray photons ($h\nu = 1486.6 \text{ eV}$). The curve fitting and linear background subtraction were carried out using the Avantage software. AFM images were obtained on a Bruker dimension icon atomic force microscope using the tapping mode. XRD experiments were conducted on a Bruker AXS (D8 ADVANCE GADDS) X-ray diffractometer with Cu K α radiation ($\lambda = 1.54 \text{ \AA}$). The beam diameter for this instrument can range from 0.05 to 0.8 mm. The density was estimated based on the mass and volume of the film. The thermoelectric power output of the 10-pair-legs TEG module was measured using a custom-made current–voltage (I – V) testing system with the temperature difference created by two metal plates as heat reservoir and two micro-thermocouples as well as electrical probes. The current and voltage outputs from two probe contacts were measured using a Keithley 2400 source meter. The I – V characteristics and power output of the transparent TEG module were measured by varying the temperature difference between the two reverse Peltier modules, which can set temperature between room temperature to 350 $^{\circ}\text{C}$. To obtain the best transparent TEG module, the leg dimension for PEDOT:PSS and ITO is 50 nm thickness \times 1 mm width and 130 nm thickness \times 0.4 mm width, respectively. The power density was determined using a thin film cross-sectional area ($5 \times 10^{-7} \text{ cm}^2$).

DATA AVAILABILITY

The authors declare that the data supporting the findings of this study are available within the paper (and its supplementary information files). Data are available upon request.

Received: 7 May 2020; Accepted: 15 July 2020;

Published online: 10 August 2020

REFERENCES

- Sofo, J. O. & Mahan, G. Optimum band gap of a thermoelectric material. *Phys. Rev. B* **49**, 4565–4570 (1994).
- Zhao, L.-D. et al. Ultralow thermal conductivity and high thermoelectric figure of merit in SnSe crystals. *Nature* **508**, 373–377 (2014).
- Heremans, J. P. et al. Enhancement of thermoelectric efficiency in PbTe by distortion of the electronic density of states. *Science* **321**, 554–557 (2008).
- Luo, Z.-Z. et al. High figure of merit in gallium-doped nanostructured n -type PbTe- x GeTe with midgap states. *J. Am. Chem. Soc.* **141**, 16169–16177 (2019).
- Luo, Y. et al. High thermoelectric performance in polycrystalline SnSe via dual-doping with Ag/Na and nanostructuring with Ag₃SnSe₆. *Adv. Energy Mater.* **9**, 1803072 (2019).
- Luo, Y. et al. n -Type SnSe₂ oriented-nanoplate-based pellets for high thermoelectric performance. *Adv. Energy Mater.* **8**, 1702167 (2018).
- Kawazoe, H. et al. p -type electrical conduction in transparent thin films of CuAlO₂. *Nature* **389**, 939–942 (1997).
- Zhang, K., Zhu, F., Huan, C. & Wee, A. Effect of hydrogen partial pressure on optoelectronic properties of indium tin oxide thin films deposited by radio frequency magnetron sputtering method. *J. Appl. Phys.* **86**, 974–980 (1999).
- Brinzari, V., Damaskin, I., Trakhtenberg, L., Cho, B. & Korotcenkov, G. Thermoelectrical properties of spray pyrolyzed indium oxide thin films doped by tin. *Thin Solid Films* **552**, 225–231 (2014).

10. Loureiro, J. et al. Transparent aluminium zinc oxide thin films with enhanced thermoelectric properties. *J. Mater. Chem. A* **2**, 6649–6655 (2014).
11. Yang, C. et al. Transparent flexible thermoelectric material based on non-toxic earth-abundant *p*-type copper iodide thin film. *Nat. Commun.* **8**, 16076 (2017).
12. Zhou, W. et al. High-performance and compact-designed flexible thermoelectric modules enabled by a reticulate carbon nanotube architecture. *Nat. Commun.* **8**, 1–9 (2017).
13. Wang, X. et al. Enhancement of thermoelectric performance of PEDOT:PSS films by post-treatment with a superacid. *RSC Adv.* **8**, 18334–18340 (2018).
14. Suarez, F. et al. Flexible thermoelectric generator using bulk legs and liquid metal interconnects for wearable electronics. *Appl. Energy* **202**, 736–745 (2017).
15. Zheng, Y., Zeng, H., Zhu, Q. & Xu, J. Recent advances in conducting poly (3, 4-ethylenedioxythiophene): polystyrene sulfonate hybrids for thermoelectric applications. *J. Mater. Chem. C* **6**, 8858–8873 (2018).
16. Bahk, J.-H., Fang, H., Yazawa, K. & Shakouri, A. Flexible thermoelectric materials and device optimization for wearable energy harvesting. *J. Mater. Chem. C* **3**, 10362–10374 (2015).
17. Kyaw, A. K. K. et al. Enhanced thermoelectric performance of PEDOT: PSS films by sequential post-treatment with formamide. *Macromol. Mater. Eng.* **303**, 1700429 (2018).
18. Jin, Y. et al. Realizing high thermoelectric performance in GeTe through optimizing Ge vacancies and manipulating Ge precipitates. *ACS Appl. Energy Mater.* **2**, 7594–7601 (2019).
19. Zheng, Y. et al. Designing hybrid architectures for advanced thermoelectric materials. *Mater. Chem. Front.* **1**, 2457–2473 (2017).
20. Shi, W. et al. Poly (nickel-ethylenetetrahiolate) and its analogs: theoretical prediction of high-performance doping-free thermoelectric polymers. *J. Am. Chem. Soc.* **140**, 13200–13204 (2018).
21. Du, Y., Xu, J., Paul, B. & Eklund, P. Flexible thermoelectric materials and devices. *Appl. Mater. Today* **12**, 366–388 (2018).
22. Scholdt, M. et al. Organic semiconductors for thermoelectric applications. *J. Electron. Mater.* **39**, 1589–1592 (2010).
23. Kim, G.-H., Shao, L., Zhang, K. & Pipe, K. P. Engineered doping of organic semiconductors for enhanced thermoelectric efficiency. *Nat. Mater.* **12**, 719–723 (2013).
24. Bubnova, O. et al. Optimization of the thermoelectric figure of merit in the conducting polymer poly (3, 4-ethylenedioxythiophene). *Nat. Mater.* **10**, 429–433 (2011).
25. Bubnova, O. & Crispin, X. Towards polymer-based organic thermoelectric generators. *Energy Environ. Sci.* **5**, 9345–9362 (2012).
26. Yakuphanoglu, F., Şenkal, B. F. & Saraç, A. Electrical conductivity, thermoelectric power, and optical properties of organo-soluble polyaniline organic semiconductor. *J. Electron. Mater.* **37**, 930–934 (2008).
27. Tang, X. et al. Notably enhanced thermoelectric properties of lamellar polypyrrole by doping with β -naphthalene sulfonic acid. *RSC Adv.* **7**, 20192–20200 (2017).
28. Hokazono, M., Anno, H. & Toshima, N. Thermoelectric properties and thermal stability of PEDOT: PSS films on a polyimide substrate and application in flexible energy conversion devices. *J. Electron. Mater.* **43**, 2196–2201 (2014).
29. Tian, R. et al. A solution-processed TiS_2 /organic hybrid superlattice film towards flexible thermoelectric devices. *J. Mater. Chem. A* **5**, 564–570 (2017).
30. Meng, Q., Jiang, Q., Cai, K. & Chen, L. Preparation and thermoelectric properties of PEDOT: PSS coated Te nanorod/PEDOT: PSS composite films. *Org. Electron.* **64**, 79–85 (2019).
31. Lu, Y. et al. Preparation and characterization of Te/poly (3, 4-ethylenedioxythiophene): poly (styrenesulfonate)/ Cu_7Te_4 ternary composite films for flexible thermoelectric power generator. *ACS Appl. Mater. Interfaces* **10**, 42310–42319 (2018).
32. Meng, Q., Cai, K., Du, Y. & Chen, L. Preparation and thermoelectric properties of SWCNT/PEDOT: PSS coated tellurium nanorod composite films. *J. Alloy. Compd.* **778**, 163–169 (2019).
33. Li, Z. et al. A free-standing high-output power density thermoelectric device based on structure-ordered PEDOT:PSS. *Adv. Electron. Mater.* **4**, 1700496 (2018).
34. Lu, Y. et al. Good performance and flexible PEDOT: PSS/ Cu_2Se nanowire thermoelectric composite films. *ACS Appl. Mater. Interfaces* **11**, 12819–12829 (2019).
35. Qu, D., Huang, X., Li, X., Wang, H. & Chen, G. Annular flexible thermoelectric devices with integrated-module architecture. *npj Flex. Electron.* **4**, 1–7 (2020).
36. Xia, Y. & Ouyang, J. Significant conductivity enhancement of conductive poly (3, 4-ethylenedioxythiophene): poly (styrenesulfonate) films through a treatment with organic carboxylic acids and inorganic acids. *ACS Appl. Mater. Interfaces* **2**, 474–483 (2010).
37. Yue, R. & Xu, J. Poly (3, 4-ethylenedioxythiophene) as promising organic thermoelectric materials: a mini-review. *Synth. Met.* **162**, 912–917 (2012).
38. Kaneko, H., Ishiguro, T., Takahashi, A. & Tsukamoto, J. Magnetoresistance and thermoelectric power studies of metal–nonmetal transition in iodine-doped polyacetylene. *Synth. Met.* **57**, 4900–4905 (1993).
39. Zhang, Q., Sun, Y., Xu, W. & Zhu, D. Thermoelectric energy from flexible P3HT films doped with a ferric salt of triflimide anions. *Energy Environ. Sci.* **5**, 9639–9644 (2012).
40. Wang, Y., Zhou, J. & Yang, R. Thermoelectric properties of molecular nanowires. *J. Phys. Chem. C* **115**, 24418–24428 (2011).
41. Mengistie, D. A. et al. Enhanced thermoelectric performance of PEDOT:PSS flexible bulky papers by treatment with secondary dopants. *ACS Appl. Mater. Interfaces* **7**, 94–100 (2015).
42. Badre, C., Marquant, L., Alsayed, A. M. & Hough, L. A. Highly conductive poly (3, 4-ethylenedioxythiophene): poly (styrenesulfonate) films using 1-ethyl-3-methylimidazolium tetracyanoborate ionic liquid. *Adv. Funct. Mater.* **22**, 2723–2727 (2012).
43. Luo, J. et al. Chemical post-treatment and thermoelectric properties of poly (3, 4-ethylenedioxythiophene):poly (styrenesulfonate) thin films. *J. Appl. Phys.* **115**, 054908 (2014).
44. Yeo, J.-S. et al. Significant vertical phase separation in solvent-vapor-annealed poly (3, 4-ethylenedioxythiophene):poly (styrene sulfonate) composite films leading to better conductivity and work function for high-performance indium tin oxide-free optoelectronics. *ACS Appl. Mater. Interfaces* **4**, 2551–2560 (2012).
45. Xia, Y., Sun, K. & Ouyang, J. Solution-processed metallic conducting polymer films as transparent electrode of optoelectronic devices. *Adv. Mater.* **24**, 2436–2440 (2012).
46. Vosgueritchian, M., Lipomi, D. J. & Bao, Z. Highly conductive and transparent PEDOT:PSS films with a fluorosurfactant for stretchable and flexible transparent electrodes. *Adv. Funct. Mater.* **22**, 421–428 (2012).
47. Kim, H. et al. Indium tin oxide thin films for organic light-emitting devices. *Appl. Phys. Lett.* **74**, 3444–3446 (1999).
48. Minami, T. Present status of transparent conducting oxide thin-film development for indium-tin-oxide (ITO) substitutes. *Thin Solid Films* **516**, 5822–5828 (2008).
49. Venkatasubramanian, R., Siivola, E., Colpitts, T. & O’quinn, B. Thin-film thermoelectric devices with high room-temperature figures of merit. *Nature* **413**, 597–602 (2001).
50. Orikasa, Y., Hayashi, N. & Muranaka, S. Effects of oxygen gas pressure on structural, electrical, and thermoelectric properties of $(\text{ZnO})_3\text{In}_2\text{O}_3$ thin films deposited by rf magnetron sputtering. *J. Appl. Phys.* **103**, 113703 (2008).
51. Ng, H., Doppalapudi, D., Moustakas, T., Weimann, N. & Eastman, L. The role of dislocation scattering in n-type GaN films. *Appl. Phys. Lett.* **73**, 821–823 (1998).
52. Kang, S. D. & Snyder, G. J. Charge-transport model for conducting polymers. *Nat. Mater.* **16**, 252–257 (2017).
53. Suwardi, A. et al. Inertial effective mass as an effective descriptor for thermoelectrics via data-driven evaluation. *J. Mater. Chem. A* **7**, 23762–23769 (2019).
54. Kim, S. J. et al. Post ionized defect engineering of the screen-printed $\text{Bi}_2\text{Te}_{2.7}\text{Se}_{0.3}$ thick film for high performance flexible thermoelectric generator. *Nano Energy* **31**, 258–263 (2017).
55. Kim, S. J., We, J. H. & Cho, B. J. A wearable thermoelectric generator fabricated on a glass fabric. *Energy Environ. Sci.* **7**, 1959–1965 (2014).

ACKNOWLEDGEMENTS

The authors acknowledge support from the A*STAR, Industry Alignment Fund, Pharos “Hybrid thermoelectric materials for ambient applications” Program (Grant nos. 1527200019 and 1527200021).

AUTHOR CONTRIBUTIONS

All authors have given approval to the final version of the manuscript. X.W., A.S., and J.X. co-wrote the manuscript with input from all authors. X.W. and J.X. conceived the idea of the experiment. Experimental data were taken by X.W., S.L.L., F.W., and A.S.

COMPETING INTERESTS

The authors declare no competing interests.

ADDITIONAL INFORMATION

Supplementary information is available for this paper at <https://doi.org/10.1038/s41528-020-00082-9>.

Correspondence and requests for materials should be addressed to X.W. or J.X.

Reprints and permission information is available at <http://www.nature.com/reprints>

Publisher's note Springer Nature remains neutral with regard to jurisdictional claims in published maps and institutional affiliations.



Open Access This article is licensed under a Creative Commons Attribution 4.0 International License, which permits use, sharing, adaptation, distribution and reproduction in any medium or format, as long as you give appropriate credit to the original author(s) and the source, provide a link to the Creative

Commons license, and indicate if changes were made. The images or other third party material in this article are included in the article's Creative Commons license, unless indicated otherwise in a credit line to the material. If material is not included in the article's Creative Commons license and your intended use is not permitted by statutory regulation or exceeds the permitted use, you will need to obtain permission directly from the copyright holder. To view a copy of this license, visit <http://creativecommons.org/licenses/by/4.0/>.

© The Author(s) 2020